CoSe$_2$ Clusters as Efficient Co-Catalyst Modified CdS Nanorod for Enhance Visible Light Photocatalytic H$_2$ Evolution

Ruizhou Gan [1,2,3], **Xiaohua Ma** [1,2,3,*], **Guorong Wang** [1,2,3] and **Zhiliang Jin** [1,2,3,*]

1   School of Chemistry and Chemical Engineering, North Minzu University, Yinchuan 750021, China
2   Ningxia Key Laboratory of Solar Chemical Conversion Technology, North Minzu University, Yinchuan 750021, China
3   Key Laboratory for Chemical Engineering and Technology, State Ethnic Affairs Commission, North Minzu University, Yinchuan 750021, China
*   Correspondence: mxh6464@163.com (X.M.); zl-jin@nun.edu.cn (Z.J.)

Abstract: CoSe$_2$, as a kind of co-catalyst, would replace noble metals element to dope pure CdS. The CoSe$_2$/CdS photocatalyst could be synthesized by simple physical mixing. With the introduction of CoSe$_2$, especially 30% CoSe$_2$/CdS, hydrogen production would be about 500 μmol within 5 h, five times that of pure CdS under the same conditions. The CoSe$_2$/CdS photocatalyst could bear four cycles of hydrogen evolution and sustain the hydrogen production, with a minor decrease. In other words, the electron transition velocity would surge along with the introduction of CoSe$_2$ particles. The CoSe$_2$ could be deemed as the predator and exit of electrons to inspire the detachment of the hole-electron pairs and relieve the recombination of the hole-electron pairs.

Keywords: CoSe$_2$ clusters; CdS nanorod; hydrogen evolution; photocatalysis

1. Introduction

A growing population and environmental deterioration face the challenge of energy diversity, instead of relying on fossil fuels. Although energy derived from fossil fuels is very strong, one cannot ignore the pollution and limited reversal of that existing in the world. Thus, mankind ought to discover some new forms of energy generation which can replace fossil fuels, resembling or even surpassing the nature of fossil energy. Recently, new energy sources, like water energy, wind energy, nuclear energy, and solar energy, have been exploited and used in everyday life, among which, solar energy and water energy are closely related to our life. As time went by, scientists came up with an idea to combine solar and water energy. Thus, except for seeking new materials, reflecting on the way of exploiting the existing resource is also an available path [1]. As the largest energy source in the world, water may soon become a promising exploitable energy source. Hydrogen, possessing four times as much fuel value as gasoline and merely leaving secure water as a secondary product, is a savior of the energy crisis in the future [2–4]. However, how to convert water into hydrogen is a confusing and troubling problem. As an exhaustless and low-cost energy, solar energy brings people the hope of sufficiently utilizing water resources. After several years, scientists believed solar energy could be stored relying on water. In 1972, Fujishima-Honda reported the hydrogen evolution effect of TiO$_2$. From that day on, more and more achievements for photocatalyst applications have been reached [5–12]. Nevertheless, the way to effectively transform solar energy into chemical energy has haunted scientists the entire way [13–15]. Therefore, photocatalysts are playing an indispensable role [16]. Unremitting efforts have been made on the study of photocatalysts ever since.

It has been found that noble metals are still the most efficient photocatalysts [17]. However, on account of the high price and intricate processing technology such metals possess, it would not be a sustainable way to squander pure noble metals. Then, metal sulfides drew the attention of scientists because of their visible-light-driven quality [18–24]. Recently, it is true that the transition-metal semiconductor CdS with a band gap of 2.4 eV embodies the potential for substituting the noble metal, featuring excellent photochemical instability and enhanced hydrogen evolution activity. Nevertheless, pure CdS usually does not show high activity in hydrogen evolution due to the quick recombination between electrons and holes, as well as the poor photocorrosion effect [25,26]. Normally, two key aspects play a vital role in the construction of hydrogen evolution systems. One is the aptly staggered band structure between semiconductors, and another is to create favorable condition for charge transfer and separation on the interface [27]. Scientists struggled to reduce the recombination between electron and hole or alleviate the photocorrosion effect. Doping other substances, such as noble metals [28–32], exhibited some prominent effect in a way. In addition, different structures and morphologies could affect hydrogen evolution a great deal [33].

These years, transition metal sulfides used as co-catalysts hve become an original method for supplementing noble metals [34–37]. Compared with pure noble metals as co-catalysts, transition metal sulfides have advantages of high efficiency and low price. Selenium, from the same family as sulfide, has similar character with sulfide [38]. That means transition metal selenides may well be a potential material for hydrogen evolution. The conduction band of $CoSe_2$ would be between the conduction band and valence band of CdS, which would accelerate the charge transfer. In this study, $CoSe_2$ was adopted to synthesize the photocatalyst by loading $CoSe_2$ to CdS nanorods through a physical method. The photocatalyst we fabricated possessed excellent hydrogen evolution activity and stability, which was qualified to adapt to more unfavorable conditions.

2. Result and Discussion

Herein, the composite of $CoSe_2$ and CdS is represented as $CoSe_2$/CdS for the co-catalyst function of $CoSe_2$ particles. Different ratios of $CoSe_2$ and CdS are exhibited as x% $CoSe_2$/CdS.

SEM was used to verify the morphology of $CoSe_2$/CdS as presented in Figure 1. As vividly presented in Figure 1b, the CdS was of a rod-like character with a linear structure in spite of how compactly the CdS nanorods were stacked. When decorated by $CoSe_2$, the CdS was still in the shape of a rod (Figure 1a). The $CoSe_2$ loaded on the surface of the CdS rod would make the surface of the CdS much more rough and jammed. The jammed area on the surface of the CdS nanorod was assigned to the $CoSe_2$ particles which confirmed the existence of active sites.

To further investigate and confirm the connection between CdS nanorods and $CoSe_2$ particles, transition electron microscopy (TEM) was used and is shown in Figure 1. As speculated before, TEM of $CoSe_2$/CdS suggested a tangible and transparent rod structure in Figure 1c, which was in line with SEM. Additionally, the square area on the surface of the CdS nanorod corresponded to $CoSe_2$ particles, which indicated that the $CoSe_2$ nanoparticles were definitely doped on the surface of CdS and the $CoSe_2$/CdS compound was successfully synthesized.

Figure 1d showed the distribution of elements on the $CoSe_2$/CdS. Apparently, the distribution of Se and Co were uniform, which certified the existence of $CoSe_2$. On the other hand, the distribution of Cd and S were uniform and constitute like rod, which confirmed the successful synthesis of CdS nanorods. Additionally, we could deduce that the size of $CoSe_2$ particles were not relatively smaller than that of CdS. The consequence was in accordance with SEM and TEM.

The HRTEM in Figure 1e showed the lattice fringe of the sample. We calculated the lattice pitch to verify the substance. As is vividly seen from the HRTEM, there are two kinds of lattice fringe in the picture. With further confirmation, 0.26 nm and 0.33 nm can be assigned to the (210) of CdS and (002) of $CoSe_2$, respectively. This consequence was in accordance with subsequent XPS and XRD.

Considering the defect of XPS in that it could only detect the element on the surface of the sample, the EDX pattern is shown in Figure 1f. S, Cd, Se, and Co were all confirmed and compensated for the blurry peak of elements presented in XPS.
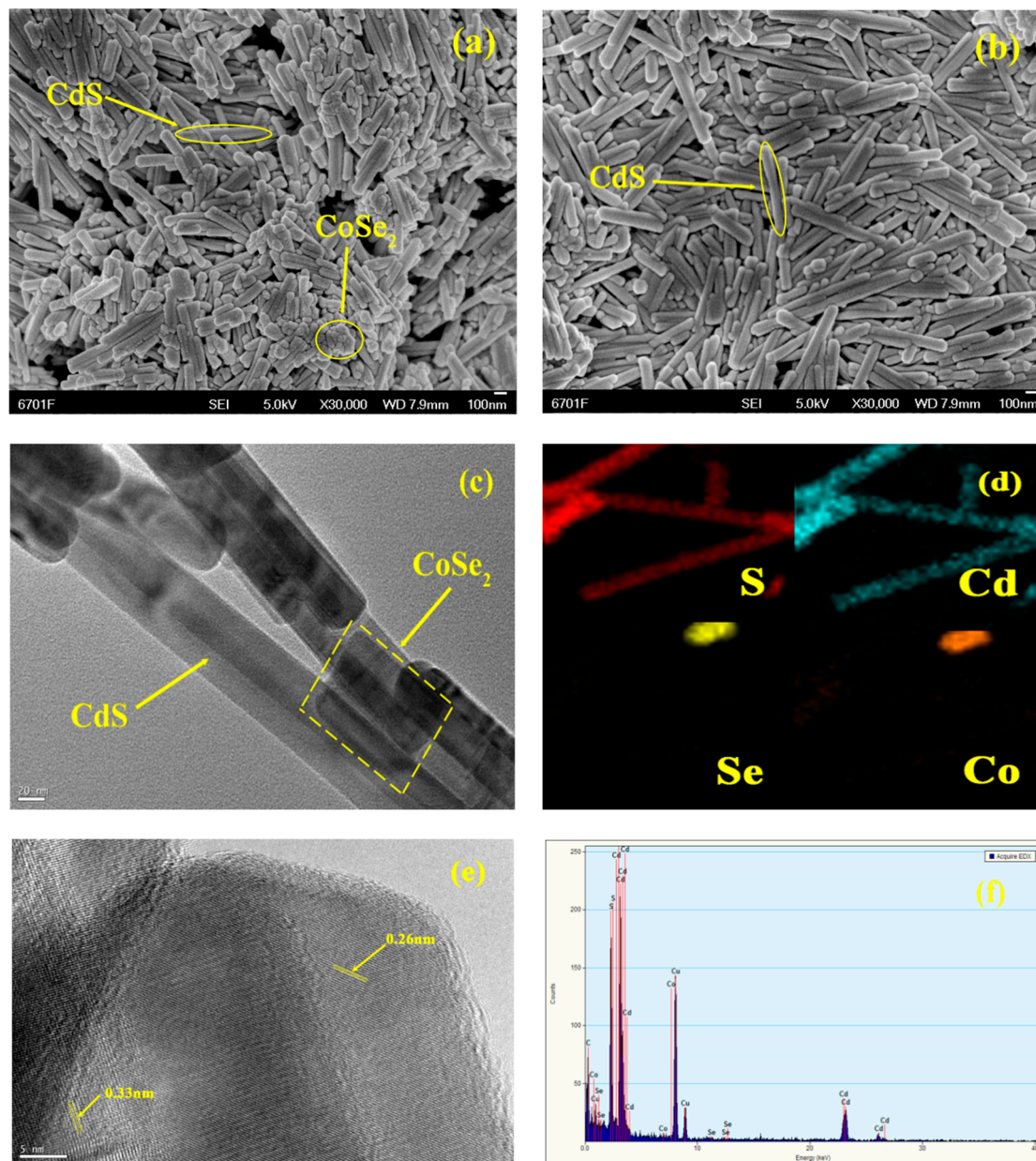

Figure 1. SEM and TEM pattern of sample: (**a**) SEM pattern of $CoSe_2/CdS$; (**b**) SEM pattern of pure CdS; (**c**) TEM pattern of 30% $CoSe_2/CdS$; (**d**) element mapping of $CoSe_2/CdS$; (**e**) the HRTEM of $CoSe_2/CdS$ sample; and (**f**) EDX pattern of $CoSe_2/CdS$.

The X-ray diffraction pattern was used to exhibit the phase structure. Results of CdS, $CoSe_2$, and $CoSe_2/CdS$ are shown in Figure 2. Observing the intense diffraction peaks of the XRD pattern, we could speculate about their high crystallinity. That is to say that the production was well crystalized as a consequence of hydrothermal treatment (JCPDS card no. 77-2306). The intense diffraction peaks corresponded to (100), (002), (101), (110), and (103) with crystals faced at 24.8°, 26.5°, 28.2°, 43.8°, 48.0°, respectively. Likewise, $CoSe_2$ had three sharp peaks at 34.2°, 37.5°, and 51.7° corresponding to (210), (211), and (311), respectively. The consequence was in good coincidence with cubic phase $CoSe_2$

(JCPDS card no. 09-0234). Afterwards, both CdS and $CoSe_2$ could be identified in the 30% $CoSe_2/CdS$, proving its definite existence and successful synthesis.
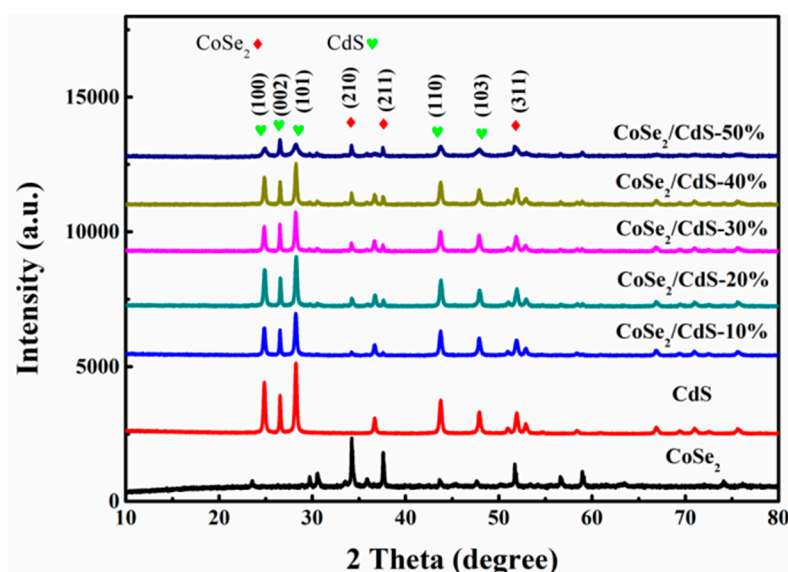

Figure 2. XRD pattern of pure CdS, $CoSe_2$ and $CoSe_2/CdS$ ranging from 10% to 50%.

To investigate the UV–VIS absorption properties of the $CoSe_2/CdS$ photocatalyst, the UV–VIS DRS was tested and the consequence of pure CdS and $CoSe_2/CdS$ is shown in Figure 3. It could be distinctively speculated from Figure 3a that the pure CdS nanorod embraced the absorption edge of around 525 nm. When pure $CoSe_2$ darkened, it absorbed the most light. After the introduction of $CoSe_2$, the $CoSe_2/CdS$ composite requires a more sufficient degree of light-absorption capability. In addition, as $CoSe_2/CdS$ was doped with the $CoSe_2$ particles, the absorption edge of $CoSe_2/CdS$ was slightly enhanced from 525 nm to 540 nm. The absorption intensity could be more obviously observed in the comparatively long wavelength. According to the Kubelka–Munk formula, the phenomenon occurred owing to the decrease of the band gap after the introduction of $CoSe_2$ particles, which showed the composite would be more prone to absorb the solar energy under same wavelength than pure CdS. The phenomenon explains the evolution of hydrogen to some extent. Additionally, we can use the Kubelka–Munk function (Figure 3b) to obtain the band gap energy of CdS, $CoSe_2$, and $CoSe_2/CdS$, respectively. With the introduction of $CoSe_2$, the band gap of $CoSe_2/CdS$ was lower than that of pure CdS, which meant the charge transfer would be easier.
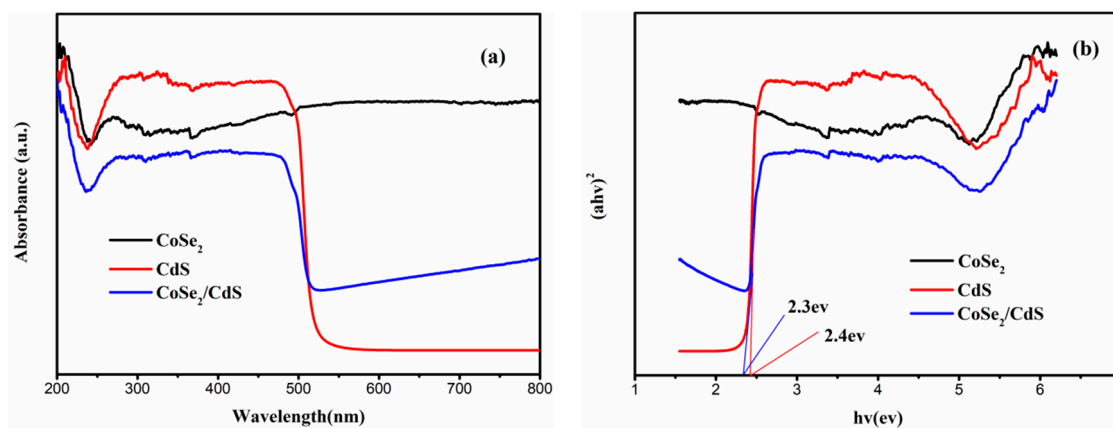

Figure 3. (**a**) The UV–VIS DRS of pure CdS, $CoSe_2$ and $CoSe_2/CdS$. (**b**) The forbidden band of CdS, $CoSe_2$, and $CoSe_2/CdS$.

For further studying the constituents of the $CoSe_2/CdS$ and verifying the elements on the surface, the XPS pattern was employed to present the contents of the catalyst. Figure 4a–d show the XPS spectra of Cd3d, S2p, Co2p, and Se3d, respectively. In Figure 4a, the main peaks of the Cd $3d_{5/2}$ and Cd $3d_{3/2}$ fell at 404.9 eV and 411.7 eV. Similarly shown in Figure 4b, the main peaks located at 161.1 eV and 162.1 eV correspond to S $2p_{3/2}$ and S $2p_{1/2}$ [39]. In the same way, the main peaks in Figure 4c, situated at 54.8 eV and 58.3 eV, correspond to Se $3d_{5/2}$ and Se $3d_{3/2}$ [40]. Finally, Figure 4d suggests that the two main peaks located at 794.68 eV and 779.3 eV, correspond to Co $2p_{3/2}$ and Co $2p_{1/2}$ [41]. The above characteristic peaks were all assigned to their corresponding elements. The result verified the existence of the pertinent elements. Therefore, the XPS specifically certified the existence of the $CoSe_2/CdS$ photocatalyst.
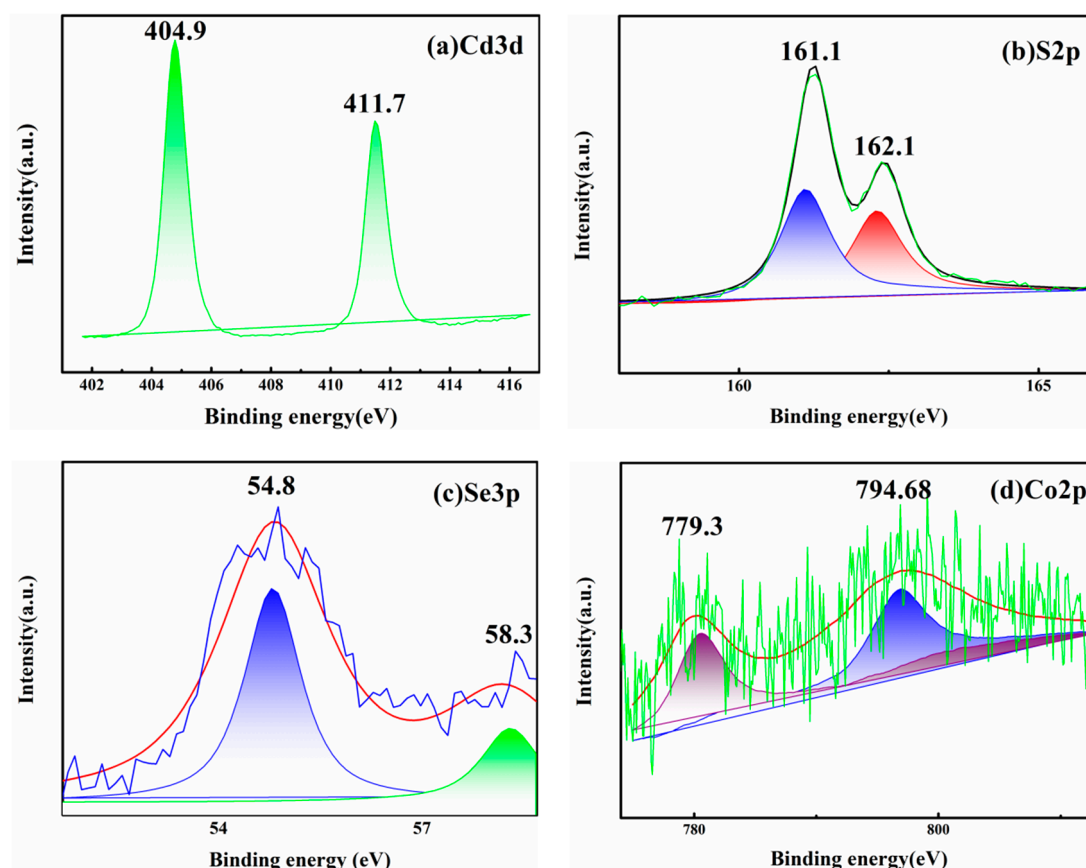

Figure 4. XPS pattern of 30% $CoSe_2/CdS$: (**a**) Cd3d; (**b**) S2p; (**c**) Se3p; and (**d**) Co2p.

To study the photocatalytic property of the $CoSe_2/CdS$ system, the $CoSe_2/CdS$ system was adopted with different ratios ranging from 10% to 50% to explore the hydrogen evolution activity under continuous visible light irradiation. The single $CoSe_2$ and CdS experiments were arranged to verify the relatively feeble hydrogen activity compared to the $CoSe_2$ doped with CdS photocatalyst. As presented in Figure 5a, the $CoSe_2$ could rarely produce H_2 in a way, which indicated pure $CoSe_2$ might not qualify as a semiconductor. Compared with pure $CoSe_2$, pure CdS had a fairly high efficiency of hydrogen evolution at 10,000 μmol/g. After doping with $CoSe_2$, the hydrogen evolution activity surged apparently. Although $CoSe_2$ did not present any semiconductor property, it actually could be a co-catalyst with in cooperation with CdS nanorods. The introduction of $CoSe_2$ particles would supply an exit for photogenerated electrons to accelerate the transition efficiency and present the phenomenon in the form of hydrogen evolution. Ranging from 10% to 50%, the increase of $CoSe_2$ could enhance the hydrogen evolution quantity and culminate at a ratio of 30% (50,000 μmol/g). Afterwards, along with the increase of $CoSe_2$, the hydrogen evolution activity declined instead. This sign indicated that

the increase of CoSe$_2$ might not merely increase the visible light absorption but also hamper the CdS nanorod from absorbing visible light. Thus, the hydrogen evolution quality reduced great deal.

On the other hand, the stability was also an essential trait which an excellent photocatalyst should possess. To solve the problem, the 30% CoSe$_2$/CdS was applied to confirm this fact. As distinctively shown in Figure 5b, the hydrogen evolution activity was steady in the first three cycles. However, along with the consumption of the lactic acid, hydrogen evolution activity apparently started to decline in the fourth cycle. This was because the remaining lactic acid could not meet the demand of the steady hydrogen evolution as the former three cycles showed. Meanwhile, photocorrosion affected the structure of the original CdS. That is to say, the function of the original CdS or CoSe$_2$ could not operate at as high an activity as before. Consequently, the 30% CoSe$_2$/CdS catalyst could sustain for three cycles but, along with the consumption of lactic acid and structural destruction arising from photocorrosion, the hydrogen evolution activity would slump a significant degree.
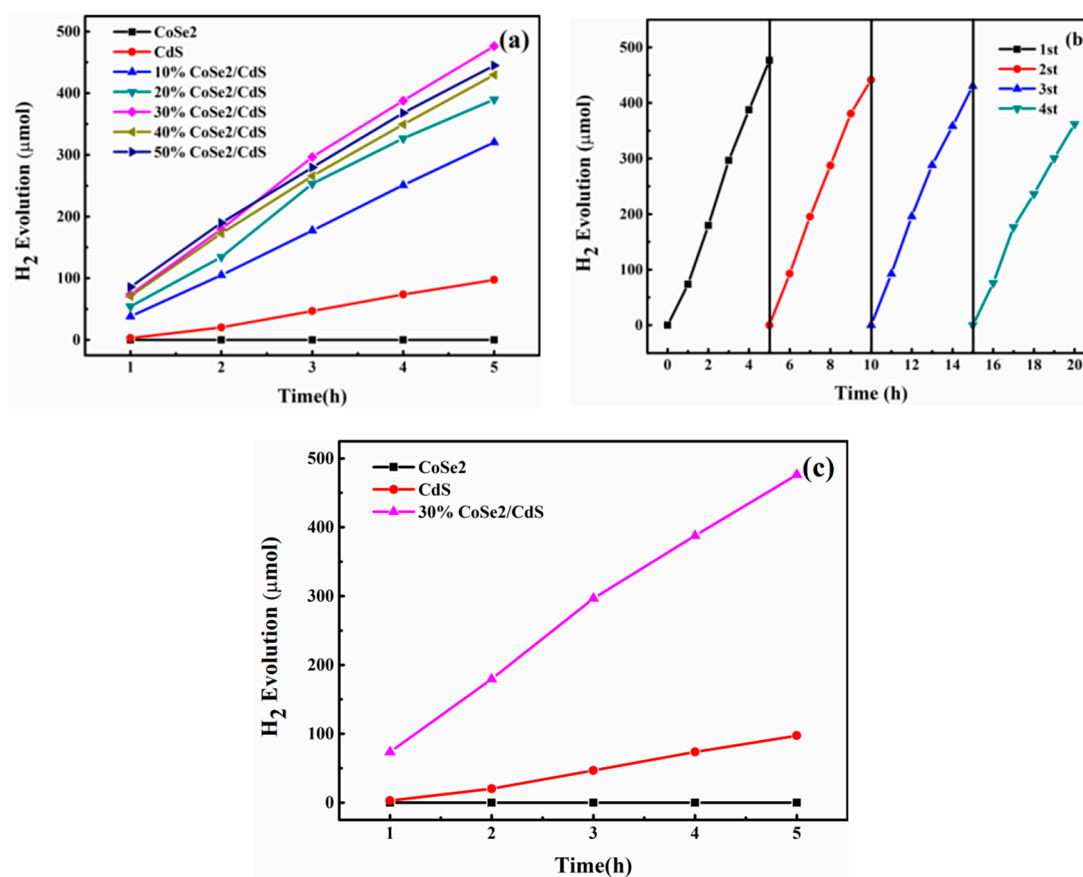

Figure 5. Research of hydrogen evolution activity: (**a**) The hydrogen evolution activity of pure CdS, CoSe$_2$ and CoSe$_2$/CdS ranging from 10–50%; (**b**) four repeating cycles of 30% CoSe$_2$/CdS; and (**c**) the hydrogen evolution compare.

For the sake of studying the mechanism during the charge transfer process of the catalysts, the photoelectrochemical attribute was confirmed in a 0.2 M Na$_2$SO$_4$ electrolyte environment. Figure 6a shows the current intensity-time curves of different catalysts in a condition under intermittent visible light illumination. With the light on and off, an evident photocurrent response presented in IT curves. The result could account for the sign of hydrogen evolution. As obviously shown in Figure 6a, pure CoSe$_2$ did not present any photocurrent response. Comparatively, pure CdS showed a relatively high current response. The above result verified the assumption made before. Gradually, along with the enhancement of CoSe$_2$ content, the photocurrent response apparently grew. Especially, the 30% CoSe$_2$/CdS catalyst exhibited the supreme photocurrent density in a parallel condition. It can be held

that the minor $CoSe_2$ particles could not support enough predators for electrons, but redundant $CoSe_2$ particles increased the burden during the electron transfer process. Ideally, this might be a process in which the separation and recombination between electrons and holes would be somehow improved.
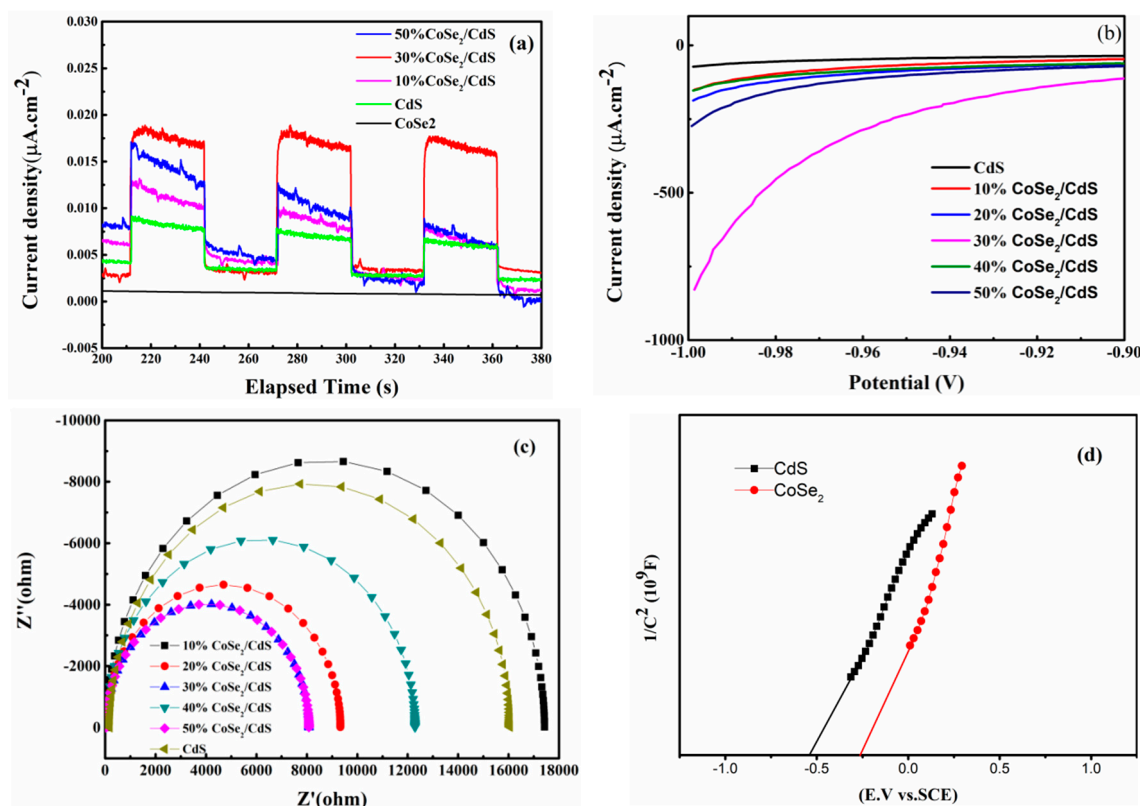

Figure 6. (**a**) The photocurrent curves of pure CdS and 10% $CoSe_2$/CdS, 30% $CoSe_2$/CdS, 50% $CoSe_2$/CdS. (**b**) LSV curves of pure CdS and $CoSe_2$/CdS ranging from 10–50%. (**c**) EIS under unilluminated condition of pure CdS and $CoSe_2$/CdS ranging from 10–50%. (**d**) Mott–Schottky plots for CdS and $CoSe_2$.

The LSV of the sample is shown in Figure 6b. As seen in the diagram, when relatively low voltage was applied to the system, a weak current response could be obtained. The reason is the H^+ around the cathode was reduced to H_2 and led to a current response. On the other hand, the sample, 30% $CoSe_2$/CdS, behaved with more positive activation than pure CdS in the same circumstance. When modified with $CoSe_2$, the sample of $CoSe_2$/CdS had a higher current response. The outcome was coincidental with former research, indicating that the $CoSe_2$/CdS composite possesses favorable charge transition efficiency and likely restrains the recombination of electrons and holes. The above result serves as evidence for the hydrogen evolution regularity.

EIS was employed to express the impedance in the catalyst electrode. Figure 6c demonstrates the EIS Nyquist curves of CdS, and different ratios of $CoSe_2$/CdS ranging from 10% to 50%, respectively. The impedance of the electrode could be reflected by the diameter of the Nyquist semicircle. The larger the radius, the larger the impedance is. It can be seen from the plot that 30% $CoSe_2$/CdS presented the minimum radius compared with the others, which meant 30% $CoSe_2$/CdS had the lowest impedance and, consequently, the 30% $CoSe_2$ boasts a better charge transition velocity. The result of EIS could confirm the charge transition quality by taking synthetic factors into account, which indirectly prove that the $CoSe_2$ particles play a significant role as a co-catalyst in the process of charge transition. We consider that the separation of electrons and holes was enhanced in some way.

The Mott–Schottky curve of the CdS and $CoSe_2$ is shown in Figure 6d. Both CdS and $CoSe_2$ exhibited positive slope, which showed that the CdS and $CoSe_2$ were both n-type semiconductor. By means of investigating the linear part of the curve, we can acquire the flat band potentials of CdS and

CoSe$_2$ via the intersection consisting of the linear partial tangent and horizontal axis. According to previous literature, the conduction band position (E$_{CB}$) of n-type semiconductors is more negative, about −0.1 V or −0.2 V, than its Efb. Meanwhile, we replace the conduction band and valence band position of the saturated calomel electrode (SCE) with the conduction band and valence band position of the normal hydrogen electrode (NHE) by Equation (1):

$$E_{NHE} = E_{SCE} + 0.241 \tag{1}$$

According to the UV–VIS band gap (Eg) data, the valence band (E$_{VB}$) position of CdS and CoSe$_2$ are calculated by Equation (2):

$$E_{CB} = E_{VB} - E_g \tag{2}$$

As presented in the Mott–Schottky curve, the CB of pure CdS was lower than that of CoSe$_2$. Thus, the CB of CoSe$_2$ was between the CB and VB of CdS, which would conduce the charge transfer. Thus, we can declare the role of CoSe$_2$ was as a co-catalyst. The consequence is shown in Table 1.

Table 1. Band gap energy, valence, and conduction band edge potential of CdS and CoSe$_2$.

Semiconductor	Band Energy Eg (eV)	Valence Band E$_{VB}$ (eV)	Conduction Band E$_{CB}$ (eV)
CdS (n-type)	2.4	2.0	−0.4
CoSe$_2$ (n-type)			−0.1

In summary, IT, LSV, and EIS curves demonstrated the obvious regularity as a pertinent photocatalyst, which was in line with the hydrogen evolution.

In order to make CoSe$_2$ have a special function in photogenic charge separation, we employed different catalysts to seek for regularity. As seen in Figure 7, the CdS was stimulated by 370 nm light so as to generate strong light fluorescence, and the maximum peak fell in the 520 nm that stimulated the catalyst from the steady-state to the first excited state along with the separation of electron-hole pairs. Nevertheless, the electrons were excited before becoming unstable. By means of the radiation transition process the electrons would decay to the ground state. In addition, energy would emit in the form of photons that produced fluorescence. Once the CoSe$_2$ was introduced to the system, PL emission exhibited a relatively intense quench phenomenon, which declared that the recombination between electrons and holes was alleviated. In particular, along with the increase of CoSe$_2$ content, notable quenching phenomenon would arise. Especially, the quenching phenomenon would culminate when the CoSe$_2$ content was adjusted to 30%, which was consistent with photocatalytic H$_2$ evolution. In this reaction process, the phenomenon would be explained as follows: CoSe$_2$ loaded on the CdS surface produced a synergistic effect and provided a swift electron transfer pathway so as to retard recombination and enhance the separation relationship between electrons and holes. Namely, the recombination of electron-hole pairs was retarded, which led to the consequence of lower fluorescence intensity. Moreover, adding CoSe$_2$ led to a slight blue shift rise in the curve, which was attributed to the quantum confinement effect. According to the Bohr radius, when the size of quantum particles closed to the exciton Bohr radius, the size reduction would restrict the movement of the current carrier, which led to the increase of kinetic energy. The originally continuous band structure would evolve to a quasi-discrete energy level, and the effective band gap of quantum dots increased with the growth of the kinetic energy. As a result, the corresponding fluorescence spectra and absorption spectra appeared to blue shift.
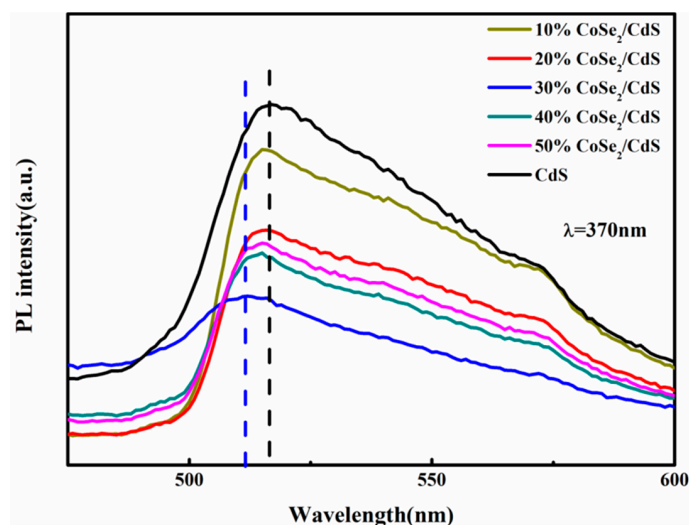
Figure 7. The PL spectra of pure CdS and CoSe$_2$/CdS ranging from 10% to 50%.

To further explore the quenching property and the optical quality in another way, fluorescence lifetime was employed by transient fluorescence spectroscopy. The consequence is shown in Table 2. Data could be acquired by following formula (3):

$$<\tau> = \sum_{i=1,2,3} B_i \tau_i^2 / \sum_{i=1,2,3} B_i \tau_i \tag{3}$$

The parameters $<\tau>$, τ_i, and B_i represent the average lifetime, decay time, and weight factors of pertinent substances, respectively. As specifically presented in Table 2, the average lifetime of CdS was 2.94 ns while, for pure CoSe$_2$, it was 0, which showed there is no semiconductor character. After doping with CoSe$_2$ particles, the average time of CoSe$_2$/CdS decreased obviously. The above results indicated that the loading of CoSe$_2$ provided an exit for photogenerated charge transfer. That was to say the fluorescent substance molecule would crash with the fluorescent quenching agent or combine in some static formation to unleash energy, so that the average time of fluorescent quenching was decreased.

Table 2. Decay parameters of pure CdS, CoSe$_2$, and CoSe$_2$/CdS ranging from 10% to 50%.

System	Lifetime $<\lambda>$ (ns)	Pre-Exponential Factor A%	Average Lifetime $<\lambda>$ (ns)	X^2
CoSe$_2$	0.0059/4.1735/153.6543	99.76/0.05/0.18	0.00	1.48080
CdS	4.1953/0.5532/79.9562	25.00/15.06/59.94	2.94	1.77483
30%	3.2128/0.4006/41.0649	27.26/15.61/57.13	2.04	1.75398

In order to determine the specific area property, the BET was a good method to characterize that of the CoSe$_2$/CdS photocatalyst. Figure 8 presents the adsorption-desorption isotherms of pure CdS nanorods and CoSe$_2$/CdS. It could be observed from Figure 8 that both of the closed curves exhibit type III isotherms, which show no inflection point and that the attraction between the photocatalyst and nitrogen is too weak at the beginning. Along with the increase of relative pressure, the amount of absorption increases greatly, which could be inferred by the seam between photocatalyst being filled in a way. Moreover, it could be also supposed that the isotherm curve of the pure CdS nanorods was above that of CoSe$_2$/CdS compound. The pertinent parameters are shown in Table 3. The S$_{BET}$, pore volume, and average pore size of CdS were 50.1874, 0.211466, and 15.1348, respectively, which were larger than that of CoSe$_2$/CdS of 13.0324, 0.39481, and 13.2311. We deduce that the larger BET parameters could be applied to more chances for nitrogen to be adsorbed. Consequently, we conclude that the decoration of CoSe$_2$ particles serving as a co-catalyst decrease the specific area and pore size but, indeed, conduce to the charge transition quality.
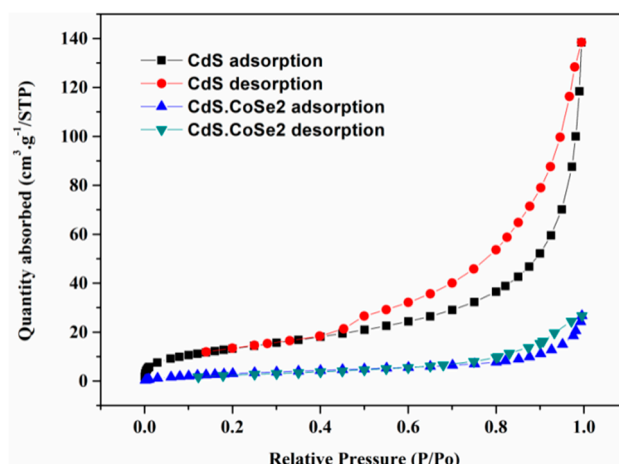
Figure 8. Nitrogen adsorption-desorption isotherms and pertinent pore size distribution curves of pure CdS nanorods and the $CoSe_2$/CdS compound.

Table 3. Nitrogen isothermal adsorption parameters.

Sample	S_{BET}/($m^2 \cdot g^{-1}$)	Pore Volume/($cm^3 \cdot g^{-1}$)	Average Pore Size/nm
CdS	50.1874	0.211466	15.1348
$CoSe_2$/CdS	13.0324	0.039481	13.2311

Referring to the previous phenomenon, the behavior of pure $CoSe_2$ in photoluminescence did not show any distinct trait as a semiconductor, so a probable mechanism for the photocatalyst over the $CoSe_2$/CdS system could be speculated. The mechanism scheme is presented in Figure 9. Firstly, the electron-hole pairs were stimulated by optical energy when exposed to invisible light. Then the electron-hole split into an electron and hole, respectively. Afterwards, the electron left the hole to move to the conduction band from the valence band. In addition, the left hole moved to the valence band and finally combined with lactic acid whereby the recombination between the electron and hole was greatly alleviated. Thus, the e^- could comfortably move to the $NiSe_2$ material and combine with H^+ to form H_2. During the process, lactic acid acted as both an electron donor and sacrificial agent. Generally speaking, the $CoSe_2$ as a co-catalyst loaded on the CdS nanorod would be employed as an electron predator to promote the transfer of electrons. Furthermore, the separation of the electron-hole would surge a great deal with the help of $CoSe_2$. Along with the improvement of electron transfer and separation of electron-holes, the hydrogen evolution activity would eventually become better.
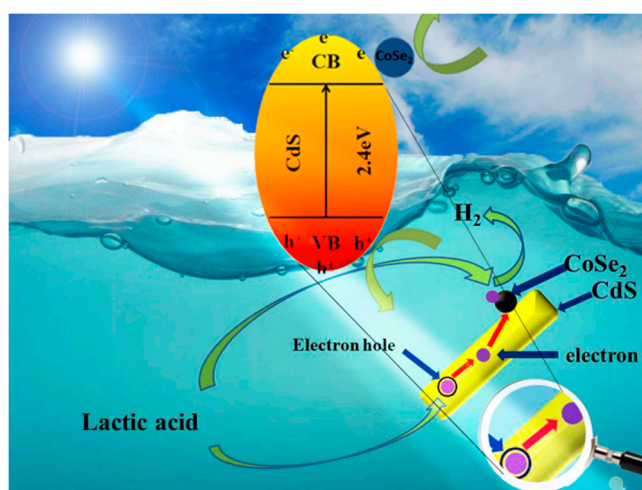

Figure 9. The mechanism of the $CoSe_2$/CdS hydrogen evolution system.

3. Experiment

3.1. Chemicals

All the reagents are of analytical grade and are used without further purification. All experiments use the deionized water. Cobalt nitrate hexahydrate ($Co(NO_3)_2 \cdot 6H_2O$) were purchased from Shanghai hutry chemical Co. LTD, lactic acid ($C_3H_6O_3$) were purchased from Shanghai Aladdin biochemical technology Co. LTD, ethylenediamine ($C_2H_8N_2$) were purchased from Yantai shuangshuang chemical Co. LTD, selenium powder (Se) and hydrazine hydrate ($N_2H_4 \cdot H_2O$) were purchased from Tianjin damao chemical reagent factory, cadmium chloride ($CdCl_2 \cdot 5/2H_2O$) were purchased from Shanghai McLean biochemical technology Co. LTD, thiourea (CH_4N_2S) were purchased from Tianjin jingu factory industrial company, ethanol (C_2H_5OH) were purchased from Sinopsin group chemical reagent Co. LTD.

3.2. Preparation of Catalysts

3.2.1. Preparation of CdS

CdS nanorods were synthesized with formerly reported ways [42]. A total of 4.63 g $CdCl_2 \cdot 6H_2O$ and 2.31 g NH_2CSNH_2 were put in a 100 mL stainless steel autoclave where 60 mL ethanediamine was already arranged. Next, the mixed solution was stirred for 30 min. Then the device was warmed at 160 °C for 36 h. Then let the autoclave cool to room temperature. Once the autoclave cooled, the precipitates were washed with deionized water and ethanol by using a centrifugal machine until the pungent smell disappeared. Next, the production was dried at 60 °C. After the product was dried, it was pounded into a fine powder by using a quartz mortar.

3.2.2. Preparation of $CoSe_2$

The method to fabricate $CoSe_2$ was similar to that of $NiSe_2$ [43]. Specifically, 2.37 g of selenium powder was mixed with 2 mL hydrazine hydrate (80%) and scattered through by being ultrasonically treated for 30 min. Then 4.36 g Co $(NO_3)_2 \cdot 6H_2O$ was added into the previous solution and was ultrasonically treated for 30 min as well to acquire a homogeneous solution. Afterwards, the solution was put into a 50 mL stainless steel autoclave and warmed at 180 °C for 24 h. Once the device cooled to ambient temperature, a centrifugal machine was used to wash and the goal product was collected with deionized water and ethanol. Finally, the sample was dried at 60 °C for 24 h, then pounded it into a fine powder in a quartz mortar.

3.2.3. Preparation of CoSe2/CdS

30% $CoSe_2$/CdS catalyst was synthesized by the following route: Firstly, 0.06 g $CoSe_2$ was spread in 20 mL ethanol; meanwhile, 0.2 g CdS was transferred into the $CoSe_2$ ethanol and was ultrasonically treated for 30 min. Next, we evaporated the ethanol in a water bath at 60 °C. Then the dried powder was washed with deionized water and ethanol by using a centrifugal machine. Afterwards, a quartz mortar was used to pound it into a fine powder. The 10% $CoSe_2$/CdS, 20% $CoSe_2$/CdS, 30%$CoSe_2$/CdS, 40% $CoSe_2$/CdS, and 50% $CoSe_2$/CdS products could be acquired by adjusting the ratio of $CoSe_2$ in the same way.

3.3. Characterization

The morphology of the production can be clearly displayed in a scanning electron microscope (JSM-6701F.JEOL). TEM distinctly exhibited on an FEI Tecnai TF20 microscope at a voltage of 200 kV. The crystalline form was identified in a Rigaku X-ray diffractometer RINT-2000. The XPS (ESCALAB 250Xi) method was applied to confirm whether the elements in the products are supposed to exist or not. UV–VIS diffuse reflectance spectra was obtained on an UV-2550 (Shimadzu) spectrometer

under $BaSO_4$ as the reference. Fluorescence quality was measured through FluoroMAX-4 spectrometer (HORIBA Scientific, France) under ambient conditions.

3.4. Photoelectrochemical Measurements

A three-electrode system can be utilized on an electrochemical workstation (CHI760E) to measure all PEC properties. The working electrode was prepared by following way: Firstly, we measured 1 mL of nafion and 9 mL of ethanol and subjected them to ultrasonic treatment to obtain the suspension liquid. Then 5 mg of photocatalyst was transferred into the suspension liquid and subject to ultrasonic treatment as well to acquire a homogeneous suspension liquid. We then placed the above liquid mixture into a FOT glass and ensured the areas on the FOT glass were the same as before, that is 1×1.5 cm^2. We then dried the product in the ambient environment. The as-prepared photoanode played the role of the working electrode and Pt plate was used as the counter electrode. Finally, a saturated calomel electrode was utilized as the reference electrode. The light source was a 300 W xenon lamp. The electrolyte employed a 0.2 mol/L Na_2SO_4 aqueous solution. Under the circumstance of intermittent cycles, 0.6 V vs. SCE biased voltage was the fixed condition.

3.5. Photocatalytic Activity Measurements

Hydrogen evolution measurements were implemented in a quartz bottle (62 mL). Hydrogen evolution was quantified according to following procedures: 10 mg catalyst powder was diffused in a 30 mL lactic acid sacrificial reagent (10% *v/v*) solution resorting to the ultrasonic method for 10 min. Being homogeneous, the system was filled with nitrogen for 5 min so as to exhaust the remaining air. Then the compounded system was put into the multichannel photocatalytic reaction apparatus. A total of 0.5 mL gas was injected through the needle per 60 min to measure the peak area of H_2 via gas chromatography. Finally, the recorded peak area was transformed into moles by referring to the standard curve for hydrogen production.

We conducted the hydrogen evolution by using the apparatus below. When we were doing the experiment, we placed the bottle in the multichannel Figure 10a and turned on the light. Then we allowed the product to absorb gas for an hour from the bottle and injected it into the gas chromatograph Figure 10b.

Figure 10. (**a**) The multichannel; (**b**) gas chromatograph.

4. Conclusions

In summary, the CdS doped with $CoSe_2$ particles possessed a hydrogen evolution efficiency of 50,000 μmol/g or so, which was five times that of pure CdS nanorods. Additionally, the $CoSe_2$/CdS photocatalyst could endure four circulation examinations of hydrogen evolution with a slight decline. On the one hand, the introduction of $CoSe_2$ would be an exit for charge transfer, as well as enhance the absorption of visible light. On the other hand, the co-catalyst would alleviate the

recombination of electrons and holes, which would contribute to the activity of hydrogen evolution. Through the photoelectrochemical, UV–VIS, and fluorescence properties, the above assumption was further confirmed.

References

1. Wang, H.; Wang, G.; Liu, Z.; Jin, Z. Strategy of nitrogen defects sponge from g-C_3N_4 nanosheets and Ni-Bi-Se complex modification for efficient dye—Sensitized photocatalytic H_2 evolution. *Mol. Catal.* **2018**, 453. [CrossRef]

2. Hao, X.; Jin, Z.; Wang, D.; Xu, J.; Min, S.; Yuan, H.; Lu, G. Behavior of Borate Complex Anion on the Stabilities and the Hydrogen Evolutions of $Zn_xCo_{3-x}O_4$ Decorated Graphene. *Superlattices Microstruct.* **2015**, *82*, 599–611. [CrossRef]

3. Li, X.; Yu, J.; Jaroniec, M. Hierarchical photocatalysts. *Chem. Soc. Rev.* **2016**, *45*, 2603–2636. [CrossRef] [PubMed]

4. Fujishima, A.; Honda, K. Electrochemical photolysis of water at a semiconductor electrode. *Nature* **1972**, *238*, 37–38. [CrossRef] [PubMed]

5. Rajeshwar, K. Hydrogen generation at irradiated oxide semiconductor solution interfaces. *J. Appl. Electrochem.* **2007**, *37*, 765–787. [CrossRef]

6. Maeda, K. Photocatalytic water splitting using semiconductor particles: History and recent developments. *J. Photochem. Photobiol. C* **2011**, *12*, 237–268. [CrossRef]

7. Hisatomi, T.; Kubota, J.; Domen, K. Recent advances in semiconductors for photocatalytic and photoelectrochemical water splitting. *Chem. Soc. Rev.* **2015**, *46*, 7520–7535. [CrossRef] [PubMed]

8. Moriya, Y.; Takata, T.; Domen, K. Recent progress in the development of (oxy)nitride photocatalysts for water splitting under visible-light irradiation. *Coord. Chem. Rev.* **2013**, *257*, 1957–1969. [CrossRef]

9. Pelaez, M.; Nolan, N.T.; Pillai, S.C. A review on the visible light active titanium dioxide photocatalysts for environmental applications. *Appl. Catal. B Environ.* **2012**, *125*, 331–349. [CrossRef]

10. Paola, A.D.; García-López, E.; Marcì, G. A survey of photocatalytic materials for environmental remediation. *J. Hazard. Mater.* **2012**, *211*, 3–29. [CrossRef]

11. Zhang, H.; Chen, G.; Bahnemann, D.W. Photoelectrocatalytic materials for environmental applications. *J. Mater. Chem.* **2009**, *19*, 5089–5121. [CrossRef]

12. Habisreutinge, S.N.; Schmidtmende, L.; Stolarczyk, J.K. Photocatalytic reduction of CO_2 on TiO_2 and other semiconductors. *Angew. Chem. Int. Ed.* **2013**, *52*, 7372–7408. [CrossRef] [PubMed]

13. Low, J.; Yu, J.; Jaroniec, M.; Wageh, S.; Al-Ghamdi, A.A. Heterojunction photocatalysts. *Adv. Mater.* **2017**, *29*, 1601694. [CrossRef] [PubMed]

14. Huang, Q.; Yu, J.; Cao, S.; Cui, C.; Cheng, B. Efficient photocatalytic reduction of CO_2 by amine-functionalized g-C_3N_4. *Appl. Surf. Sci.* **2015**, *358*, 350–355. [CrossRef]

15. Tong, H.; Ouyang, S.; Bi, Y.; Umezawa, N.; Oshikiri, M.; Ye, J. Nano-photocatalytic materials: Possibilities and challenges. *Adv. Mater.* **2012**, *24*, 229–251. [CrossRef] [PubMed]

16. Schneider, J.; Matsuoka, M.; Takeuchi, M.; Zhang, J.; Horiuchi, Y.; Anpo, M.; Bahnemann, D.W. Understanding TiO_2 photocatalysis: Mechanisms and materials. *Chem. Rev.* **2014**, *114*, 9919–9986. [CrossRef] [PubMed]

17. Ye, R.; Fang, H.; Zheng, Y.Z.; Li, N.; Wang, Y.; Tao, X. Fabrication of $CoTiO_3$/g-C_3N_4 hybrid photocatalysts with enhanced H_2 evolution: Z-scheme photocatalytic mechanism insight. *ACS Appl. Mater. Inter.* **2016**, *8*, 13879–13889. [CrossRef]

18. Linsebigler, A.L.; Lu, G.; Yates, J.T. Photocatalysis on TiO_2 surfaces: Principles, mechanisms, and selected results. *Chem. Rev.* **1995**, *95*, 735–758. [CrossRef]

19. Yu, J.; Zhang, J.; Liu, S. Ion-exchange synthesis and enhanced visible-light photoactivity of CuS/ZnS nanocomposite hollow spheres. *J. Phys. Chem. C.* **2010**, *114*, 13642–13649. [CrossRef]

20. Yu, J.; Zhang, J. A simple template-free approach to TiO_2 hollow spheres with enhanced photocatalytic activity. *Dalton Trans.* **2010**, *39*, 5860–5867. [CrossRef]

21. Zhang, J.; Yu, J.; Jaroniec, M. Noble metal-free reduced graphene oxide-$Zn_xCd_{1-x}S$ nanocomposite with enhanced solar photocatalytic H_2 production performance. *Nano Lett.* **2012**, *12*, 4584–4589. [CrossRef] [PubMed]

22. Yu, J.; Yang, B.; Cheng, B. Noble-metal-free carbon nanotube $Cd_{0.1}Zn_{0.9}S$ composites for high visible-light photocatalytic H_2 production performance. *Nanoscale* **2012**, *4*, 2670–2677. [CrossRef] [PubMed]

23. Xiang, Q.; Yu, J.; Jaroniec, M. Synergetic effect of MoS_2 and graphene as cocatalysts for enhanced photocatalytic H_2 production activity of TiO_2 nanoparticles. *J. Am. Chem. Soc.* **2012**, *134*, 6575–6578. [CrossRef] [PubMed]

24. Li, Q.; Guo, B.; Yu, J. Highly efficient visible-light-driven photocatalytic hydrogen production of CdS-cluster-decorated graphene nanosheets. *J. Am. Chem. Soc.* **2011**, *133*, 10878–10884. [CrossRef] [PubMed]

25. Zhang, Y.; Jin, Z.; Yuan, H.; Wang, G.; Ma, B. Well-regulated Nickel nanoparticles functional modified ZIF-67 (Co) derived Co_3O_4/CdS p-n heterojunction for efficient photocatalytic hydrogen evolution. *Appl. Surf. Sci.* **2018**, *462*, 213–225. [CrossRef]

26. Yan, X.; Liu, X. Antiphotocorrosive photocatalysts containing CdS nanoparticles and exfoliated TiO_2 nanosheets. *J. Mater. Res.* **2010**, *25*, 182–188. [CrossRef]

27. Fu, J.; Xu, Q.; Low, J.; Jiang, C.; Yu, J. Ultrathin 2D/2D WO_3/gC_3N_4 step-scheme H_2-production photocatalyst. *Appl. Catal. B Environ.* **2019**, *243*, 556–565. [CrossRef]

28. Qi, L.; Yu, J.M.; Jaroniec, M. Preparation and enhanced visible-light photocatalytic H_2-production activity of CdS-sensitized Pt/TiO_2 nanosheets with exposed (001) facets. *Chem. Chem. Phys.* **2011**, *13*, 8915–8923. [CrossRef]

29. Li, B.; Wang, Y. Synthesis, microstructure, and photocatalysis of ZnO/CdS nano heterostructure. *J. Phys. Chem. Solids* **2011**, *72*, 1165–1169. [CrossRef]

30. Xu, L.; Shi, W.; Guan, J. Preparation of crystallized mesoporous CdS/Ta_2O_5, composite assisted by silica reinforcement for visible light photocatalytic hydrogen evolution. *Catal. Commun.* **2012**, *25*, 54–58. [CrossRef]

31. Wang, Y.; Wang, Y.; Xu, R. Photochemical deposition of Pt on CdS for H_2 evolution from water: Markedly enhanced activity by controlling Pt reduction environment. *J. Phys. Chem. C* **2012**, *117*, 783–790. [CrossRef]

32. Wu, K.; Zhu, H.; Zheng, L. Ultrafast charge separation and long-lived charge separated state in photocatalytic CdS–Pt nanorod heterostructures. *J. Am. Chem. Soc.* **2012**, *134*, 10337–10340. [CrossRef] [PubMed]

33. Hao, X.; Jin, Z.; Yang, H.; Lu, G.; Bi, Y. Peculiar Synergetic Effect of MoS_2 Quantum Dots and Graphene on Metal-Organic Frameworks for Photocatalytic Hydrogen Evolution. *Appl. Catal. B Environ.* **2017**, *210*, 45–56. [CrossRef]

34. Zhang, Y.; Peng, Z.; Guan, S. Data on the synthesis processes optimization of novel β-NiS film modified CdS nanoflowers heterostructure nanocomposite for photocatalytic hydrogen evolution. *Data Brief* **2018**, *16*, 828–842. [CrossRef] [PubMed]

35. Liu, J.; Fang, W.; We, Z. Metallic 1T-Li_xMoS_2 Co-catalyst enhanced photocatalytic hydrogen evolution over $ZnIn_2S_4$ floriated microspheres under visible light irradiation. *Catal. Sci. Technol.* **2018**, *8*, 1375–1382. [CrossRef]

36. Jian, W.; Bo, L.; Chen, J. Enhanced photocatalytic H_2-production activity of $Cd_xZn_{1-x}S$ nanocrystals by surface loading MS (M = Ni, Co, Cu) species. *Appl. Surf. Sci.* **2012**, *259*, 118–123.

37. Chen, T.; Song, C.; Fan, M. In-situ fabrication of CuS/g-C_3N_4, nanocomposites with enhanced photocatalytic H_2 production activity via photoinduced interfacial charge transfer. *Int. J. Hydrogen Energy* **2017**, *42*, 12210–12219. [CrossRef]

38. Chhowalla, M.; Shin, H.; Eda, G.; Li, L.; Loh, K.; Zhang, H. The chemistry of twodimensional layered transition metal dichalcogenide nanosheets. *Nat. Chem.* **2013**, *5*, 263–275. [CrossRef]

39. Yang, H.; Jin, Z.; Hu, H.; Lu, G.; Bi, Y. Fabrication and behaviors of CdS on Bi_2MoO_6 thin film photoanodes. *RSC Adv.* **2017**, *7*, 10774–10781. [CrossRef]

40. Jarimavičiūtė-Žvalionienė, R.; Tamulevičius, S.; Andrulevičius, M.; Tomašiūnas, R.; Grigaliūnas, V. Photoluminescence and XPS Study of Selenium Treated Porous Silicon. In *Nanostructured and Advanced Materials for Applications in Sensor, Optoelectronic and Photovoltaic Technology*; Springer: Berlin/Heidelberg, Germany, 2005; pp. 371–374.

41. Liu, D.; Jin, Z.; Bi, Y. Charge transition channel construction between a MOF and rGO by means of Co-Mo-S modification. *Catal. Sci. Technol.* **2017**, *7*, 4478–4488. [CrossRef]

42. Jang, J.; Joshi, U.A.; Lee, J.S. Solvothermal synthesis of CdS nanowires for photocatalytic hydrogen and electricity production. *J. Phys. Chem. C* **2007**, *111*, 13280–13287. [CrossRef]

43. Wang, S.; Li, W.; Xin, L. Facile synthesis of truncated cube-like NiSe$_2$, Single crystals for High-performance asymmetric supercapacitors. *Chem. Eng. J.* **2017**, *330*, 1334–1341. [CrossRef]